



POLITECNICO
MILANO 1863

DIPARTIMENTO DI MECCANICA



Additively manufactured iron-manganese for biodegradable porous load-bearing bone scaffold applications

Carluccio, D.; Xu, C.; Venezuela, J.; Cao, Y.; Kent, D.; Bermingham, M.; Demir, A. G.; Previtali, B.; Ye, Q.; Dargusch, M.

This is a post-peer-review, pre-copyedit version of an article published in ACTA BIOMATERIALIA. The final authenticated version is available online at:

<http://dx.doi.org/10.1016/j.actbio.2019.12.018>

This content is provided under [CC BY-NC-ND 4.0](https://creativecommons.org/licenses/by-nc-nd/4.0/) license



Additively Manufactured Iron-Manganese for Biodegradable Porous Load-Bearing Bone Scaffold Applications

Danilo Carluccio^{a,b,1,†}, Chun Xuc, [†], Jeffrey Venezuela^{a,b}, Yuxue Caoc, Damon Kent^{a,b,d}, Michael Bermingham^{a,b}, Ali Gökhan Demir^e, Qingsong Yec, Barbara Previtalie, Matthew Dargusch^{a,b,1}

^a School of Mechanical and Mining Engineering and Queensland Centre for Advanced Materials Processing and Manufacturing (AMPAM), The University of Queensland, Australia

^b Australian Research Council Research Hub for Advanced Manufacturing of Medical Devices

^c School of Dentistry, The University of Queensland, Brisbane, Queensland, 4006, Australia

^d School of Science and Engineering, University of the Sunshine Coast, Maroochydore DC, QLD 4558, Australia

^e Department of Mechanical Engineering, Politecnico di Milano, Via La Masa 1, 20156 Milan, Italy

Abstract

Selective laser melting (SLM) can produce complex hierarchical architectures paving the way for highly customisable biodegradable load-bearing bone scaffolds. For the first time, an in-depth analysis on the performance of SLM-manufactured iron-manganese bone scaffolds suitable for load-bearing applications is presented. Microstructural, mechanical, corrosion and biological characterisations were performed on SLM-manufactured iron-manganese scaffolds. The microstructure of the scaffold consisted primarily of γ -austenite, leading to **high** ductility. The mechanical properties of the scaffold were sufficient for load-bearing applications even

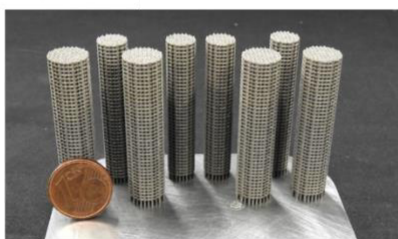
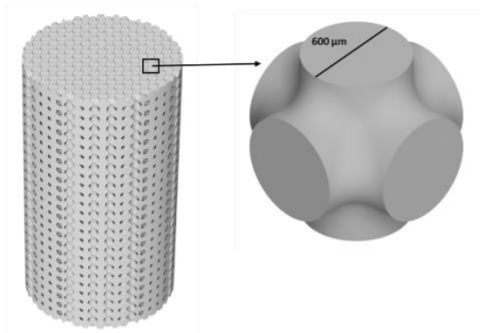
[†] CX and DC contributed equally to this work.

¹ Corresponding authors: d.carluccio@uq.edu.au, m.dargusch@uq.edu.au

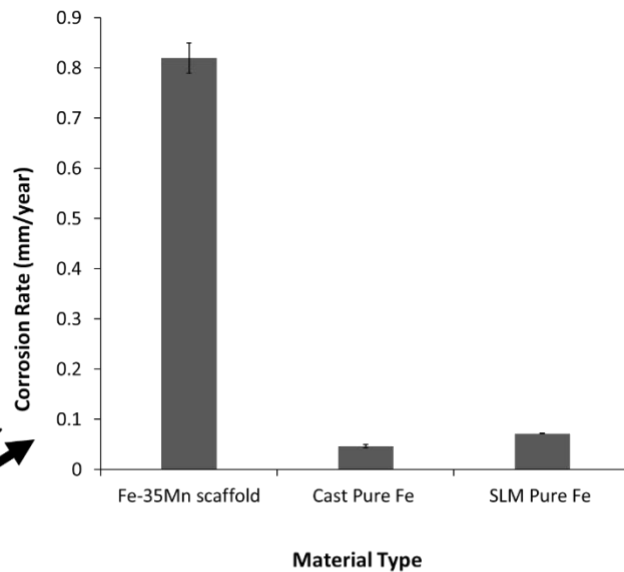
after 28 days immersion in simulated body fluids. Corrosion tests showed that the corrosion rate was much higher than bulk pure iron, attributed to a combination of the manufacturing method, the addition of Mn to the alloy and the design of the scaffold. *In vitro* cell testing showed that the scaffold had good biocompatibility and viability towards mammalian cells. Furthermore, the presence of filopodia showed good osteoblast adhesion. *In vivo* analysis showed successful bone integration with the scaffold, with new bone formation observed after 4 weeks of implantation. Overall the SLM manufactured porous Fe-35Mn implant showed promise for biodegradable load-bearing bone scaffold applications.

Graphical Abstract

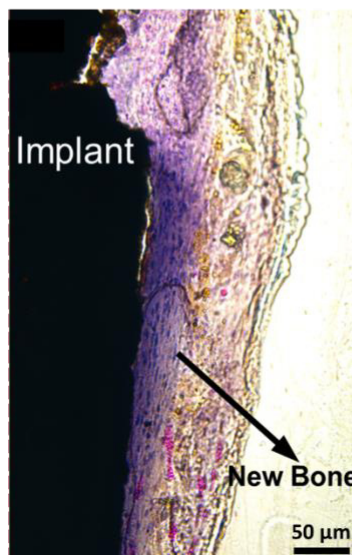
Additively Manufactured Fe-35Mn Scaffold



Improved
corrosion rate



Successful *in vivo*
bone integration
and new bone
formation



Keywords

Selective Laser Melting; Biodegradable Iron; Bone Scaffolds; *in vivo* testing; biological characterisation; corrosion testing; mechanical characterisation

1.0 Introduction

Critical bone defects (CBD) almost always require surgical intervention; typically, if a gap in the bone is greater than 30 mm it will not entirely heal on its own [1]. If the CBD is in a location that sustains forces, then load-bearing scaffolds are a suitable treatment method. Load-bearing bone scaffolds provide a 3-D structure that fills the CBD and allows for cell seeding, attachment, and proliferation leading to bone regeneration [2]. An ideal load-bearing bone scaffold should:

- be fully biocompatible and preferably osteoconductive [3];
- be completely biodegradable leaving behind no residue [4];
- have hierarchical porosity with suitable pore sizes to allow for the flow of oxygen, nutrients and waste products [5];
- have sufficient mechanical properties to match the bone at the implantation site and allow for appropriate load transfer during ameliorating [5].

Bone scaffolds manufactured from polymers and ceramics have been shown to have good biocompatibility, biodegradability, and encourage bone growth [6]. There are some concerns with the inflammatory responses from traditional biodegradable polymers due to acidic degradation and resorption of the by-product, which is exacerbated in orthopaedic conditions due the low vascularization and metabolic activity [6]. Over the last decade, advances in bone scaffolds have seen both polymer, ceramic and polymer-ceramic hybrids used clinically [7]. However, their mechanical properties are generally not sufficient to allow for the repair of load-bearing bone [8]. On the other hand, permanent metallic scaffolds manufactured from tantalum [9], cobalt-chromium (CoCr) [10] and titanium alloys [11] have high mechanical

properties; often too high compared to the host bone, resulting in stress shielding that causes bone resorption [12]. Furthermore, the permanent nature of these materials requires a second surgery to remove the scaffold, or if left in the body for a prolonged period, could release toxic ions resulting in peri-implant cell death and bone atrophy [13].

For these reasons, biodegradable metals (BDM) have garnered significant interest as they have been shown to overcome the disadvantages of other bone scaffold materials. BDM are defined as metals that corrode gradually in the body with a suitable host response to their implantation and subsequent corrosion [14]. The bulk corrosion product of BDM should be an essential element the body can metabolise successfully in large doses [15]. Secondary corrosion products should be non-toxic and easy to metabolise. An ideal BDM should have suitable mechanical properties for load-bearing applications, and during healing, retain its mechanical properties and slowly degrade, transferring the stress to the newly formed bone without damaging it; subsequent to full healing, the implant would completely dissolve away leaving behind no residue. Essential metallic macronutrients include: calcium (Ca), magnesium (Mg), sodium (Na), potassium (K), iron (Fe) and zinc (Zn), [16] of these Mg, Fe and Zn based alloys have been the most widely researched BDM [14].

Magnesium has been extensively researched as a BDM for orthopaedic applications, as it has a density close to that of bone [17], has been shown to promote osteogenesis [18] and has a modulus closer to that of bone when compared to the Zn and Fe based alloys [17]. However, Mg can be difficult to manufacture traditionally due to its formability [19]. **Furthermore, mechanical integrity during bone fixation and subsequent bone healing may not be sufficient due to the higher corrosion rate of Mg [14]. Mg-based implants have been shown to have**

adequate corrosion rate for bulk orthopaedic fixation devices (such as screws) and have been made commercially available [20]. However, for porous implants, since a higher surface area is exposed to the environment a faster corrosion rate occurs compared to bulk implants, resulting in a faster loss of mechanical integrity over time, and thus are currently unsuitable for load-bearing applications [21]. Moreover, in orthopaedic applications where blood flow, and consequently mass transport, is minimal, the hydrogen evolution that occurs during the degradation of corrosion can result in gas pockets causing tissue cavities [18] and damage to the healing bone [22].

Zinc, on the other hand, has a favourable and more controllable corrosion rate for biodegradable implants and exhibits good biocompatibility [23, 24]. However, the mechanical properties of Zn are often regarded as insufficient for load-bearing applications [24]. Mechanical properties are expected to be further compromised by the presence of a porous structure since pores act as stress concentrators, as confirmed by studies on porous Zn and Zn alloys by Capek et al. [25] and Hou et al. [26]. Hence, porous Zn implant would be limited to those applications where tensile loading is not significant and compressive loading dominates (e.g., dental applications).

Compared to Mg and Zn, Fe has much higher hardness, strength and ductility, similar to that of 316L stainless steel [27]. The good combination of strength and ductility in Fe will be especially useful as this allows the possibility of maintaining acceptable mechanical properties despite the presence of volume defects and, thereby, expands the applicability of the porous construct. As is true for most elements, Fe can be toxic in high doses; however, iron toxicity is usually rare since iron levels are regulated through absorption rather than

secretion as is the case with Zn [28]. However, the *in vivo* degradation rate of pure iron is regarded as being too slow and hence can invoke similar inflammatory responses as permanent metallic implants [29]. Pure Fe is also ferromagnetic which can impede magnetic resonance imaging (MRI). Alloying with sufficient Mn promotes austenitic phase growth, improving MRI compatibility and formability [27, 30]. Additionally, when alloyed with Fe with it has been shown to increase the degradation rate compared to pure Fe [30, 31]. For these reasons, Fe-Mn based systems have been the most researched biodegradable iron alloys [30, 32]. Hermawan et al. and Dargusch et al. have shown that additions of 35 weight percent Mn resulted in **good** mechanical properties, high degradation rates and good biocompatibility [27, 30].

Selective laser melting (SLM) can produce implants with complex hierarchical architectures not possible by traditional manufacturing methods, which is ideal for bone scaffolds [33]. The typical properties of BDM can render them difficult to SLM; for example, Mg is highly volatile and flammable, especially in powder form, causing safety concerns for SLM processing. Nonetheless, magnesium scaffolds have been successfully manufactured using SLM [21]. However, as discussed above, this is problematic for Mg bone scaffolds as the porous nature of the implant results in a higher degradation rate compared to bulk counterparts [21]. Similarly, while less flammable than Mg, the relatively small difference between the melting point and boiling point of Zn [34] renders it difficult to process via SLM [34]. While Zn scaffolds have been successfully produced, the evaporative recoil force caused problems for the surface roughness and processing porosity [35]. On the other hand, while Fe and Fe based alloys are relatively easy to process via SLM [36, 37], the majority of research has focused on maraging, tool and other specialty steels used in industry [38]. There is a lack of knowledge on Fe-based biodegradable bone scaffold, with only one study fully

characterising pure Fe scaffolds manufactured using SLM [39]. This study is the first to investigate whether SLM-manufactured iron-manganese scaffolds are suitable for load-bearing scaffold applications, by providing a comprehensive study on the mechanical properties, biodegradation, *in vitro* and *in vivo* biocompatibility of the scaffolds for load-bearing applications.

2.0 Materials and Method

2.1 Scaffold Manufacturing

Scaffolds were manufactured using the same gas atomised spherical Fe-35Mn powder (CEAIT, San Sebastian, Spain) with the same composition, morphology and particle size distribution ($\leq 44 \mu\text{m}$) as used in previous studies [40].

The scaffolds design was based on Schwarz Primitive Surface p-unit cells (Figure 1 A-B), which have been shown to be highly suitable for bone scaffold applications owing to the high strength-to-weight ratio and outstanding fluid permeability and stress distribution [41]. The scaffolds were designed to have a maximum pore size of $400 \mu\text{m}$, a maximum strut size of $600 \mu\text{m}$, and an overall porosity of 42 %.

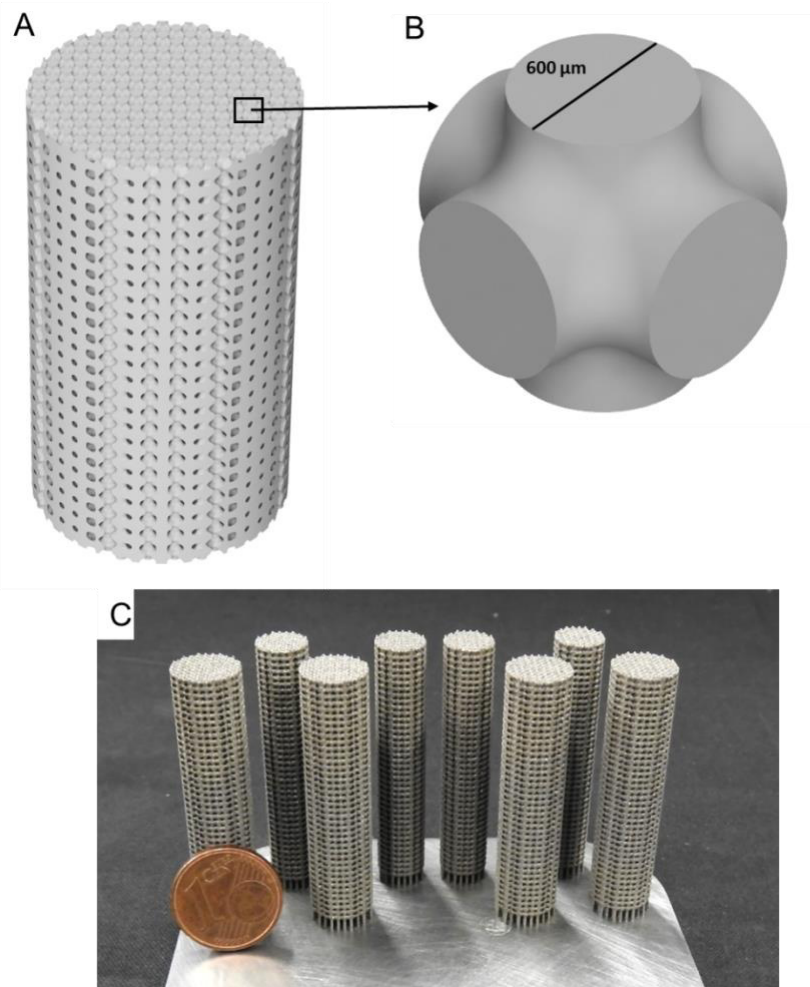


Figure 1 (A) CAD of scaffold, (B) Repeating unit cell, (C) As manufactured scaffold.

Cylindrical scaffolds were manufactured on a mild steel baseplate using a Renishaw AM250 SLM system fitted with a reduced build volume (Renishaw, Stone, UK). Scaffolds were processed using parameters based on previous studies [40], with a layer thickness of 50 μm, peak power of 125W, pulse duration of 50 μs and point distance and hatch distance of 45 μm. Magics 19 (Materialise, Leuven, Belgium) was used to prepare the build and assign processing parameters.

Preceding lattice manufacturing, the SLM chamber was evacuated to -950 mbar followed by flooding with argon until an overpressure of 15 mbar was achieved. Processing occurred under Ar atmosphere with oxygen content held below 1000 ppm. As built samples are shown in Figure 1 C. **Following the build scaffolds were ultrasonically cleaned for 30 minutes in pure ethanol (hereafter referred to as ethanol).** For mechanical, electrochemical and immersion testing samples were machined to size followed by ultrasonic cleaning for 30 minutes in ethanol. Before every test, samples were ultrasonically cleaned again in ethanol for 10 minutes.

The processed density of the scaffolds was measured using micro-CT and dry weight in air. Micro-CT was performed using an Inveon preclinical micro-CT scanner (Siemens, Berlin, Germany) with an 80 kV voltage, 150 μ A current, 4000 ms exposure time, and 16.5 μ m effective pixel size. The scans were performed using 360° rotation with 360 rotation steps with a high magnification and a binning factor of two. The images were reconstructed on an Inveon Acquisition Workstation software (IAW version 2.4, Siemens) using a Feldkamp reconstruction software (Siemens). Porosity analysis was done using BoneJ [42].

Using the dry weight in air measurements, the porosity percentage of the scaffolds was calculated using:

$$\rho(\%) = \left(1 - \frac{M_{air}}{M_{ideal}}\right) \cdot 100 \quad (1)$$

Where M_{air} is the mass of scaffold in air and M_{ideal} is the theoretical mass of a solid cylinder of the same material with same diameter and height. Measurements were repeated three times on three different samples.

Table 1 Percentage Porosity of Fe-35Mn Scaffold

	Designed	μ CT	Dry Weight
Porosity (%)	42.3	43.1 ± 0.9	42.6 ± 0.2

2.2 Material Characterization

As-built scaffold surfaces were observed under SEM (TM3030, Hitachi, Japan).

Metallographic cross sections were obtained by cutting samples perpendicular and parallel to the build direction, cold mounting, grinding and mechanically polishing following standard metallographic procedures. These were observed under optical microscopy to reveal a processed density of the struts over 99.5%. Nital solution was used to etch the samples to show the microstructure. The microstructure was observed using optical microscopy (Polyvar Met, Reichert, USA) and SEM.

Phase identification was performed on the scaffolds using XRD (Aeris Research, Malvern Panalytical, Netherlands) using Cu $K\alpha$ radiation with a voltage of 40kV and current of 15mA, step size of 0.02° and a scan range (2θ) from $35-85^\circ$. XRD was performed with build direction out of plane.

Chemical composition of the scaffold was analysed using inductively coupled plasma atomic emission spectroscopy (ICP-AES) and is given in below.

Table 2 Chemical composition of scaffold.

Material	Fe	C	Mn	Si	S	P	Ni	Cr	Mo
Fe-35Mn	Bal.	0.03	33.0	0.06	0.01	<0.01	0.01	0.03	<0.01

Uniaxial compression testing was based on ISO 13314 [43] and performed at room temperature on flat, hard, parallel plates with a crosshead speed of 2 mm/min to 30% strain, which was measured using a video extensometer (Shimadzu AGS-100kNX, Kyoto, Japan). Scaffolds were machined to have a height-to-diameter ratio of 1.75. Stress calculations were done using the nominal area.

2.3 Electrochemical Testing

The electrochemical performance of the Fe-35Mn scaffolds was evaluated using potentiodynamic polarisation tests based on ASTM G59-97 [44]. Samples were cut perpendicular to the build direction, and cold mounted in epoxy resin. Care was taken to ensure that the scaffold was fully impregnated with the resin so that only the metal on the surface was exposed to the testing environment. This way the true surface area can be measured to avoid inaccurate corrosion rates (if the true surface area exposed to the environment is larger than the estimated surface area then the calculated corrosion rate will be significantly higher than the real corrosion rate since more metal is exposed to the environment than predicted). The specimens were then connected to a copper wire and

subsequently polished to 1200 grit and ultrasonically cleaned with ethanol. Optical microscopic images were taken of the exposed surface to be tested to ensure that the epoxy had fully infiltrated the pores. Following this image processing software was used to determine the surface area of the exposed metal. To reduce the exposure time of the testing surface to the atmosphere special care was taken to reduce the time between surface polishing and testing.

Testing was done using a standard three-electrode cell (PARSTAT 2263, Princeton Applied Research, USA) with a silver/silver chloride/saturated potassium chloride electrode, platinum counter-electrode and the specimen as the working electrode. Experiments were performed at a temperature of 37 ± 1 °C with the solution freshly prepared half an hour before each test to allow it to reach 37 ± 1 °C. A standard Hank's balanced salt solution (pH 7.2 to 7.4) was prepared by mixing commercial HBSS powder (Sigma-Aldrich H1387: 8.0 g NaCl, 0.14 g CaCl₂, 0.4 g KCl, 1.0 g glucose, 0.048 g Na₂HPO₄ (anhydrous), 0.06 g KH₂PO₄ (anhydrous), 0.097 g MgSO₄ (anhydrous)) with 0.353 g sodium bicarbonate for a 1-liter solution. HBSS is a close serum analogue of blood plasma without the protein components. Following immersion of the samples, the open circuit potential (OCP) was measured for 150 minutes to allow for surface stabilisation of the working electrode. After OCP, electrochemical impedance spectroscopy (EIS) was completed with a scanning frequency ranging between 100 kHz and 10 mHz employing a single sine acquisition mode with an applied amplitude of 10 mV. Next, linear polarisation testing was done using a scan rate of 0.166 mV/s and applied potential of ± 0.25 V (vs. SCE). The corrosion rate was determined using the following equation from ASTM G59-97 [44]:

$$CR_e = 3.27 \times 10^{-3} \frac{i_{corr}EW}{\rho} \quad (2)$$

Where CR_e is the corrosion rate, i_{corr} is the corrosion current density, EW is the equivalent weight and ρ is the theoretical density of Fe-35Mn. An EW of 27.9 g/eq based on the reaction $Fe \rightarrow Fe^{2+}$ and theoretical density of 7.63 g/cm³ was used for CR calculations [27].

2.3 Immersion Testing

Prior to testing, sample surfaces were ground to 1200 grit followed by ultrasonic cleaning in ethanol for 15 minutes. Subsequently, samples were measured and weighed. **Immersion testing was performed in quasi-static conditions, using the test apparatus as described in detail by Johnston et al [45]. Samples were immersed for 28 days, as recommended by ASTM-A31-12a, in Hank's balanced salt solution with added 0.353 g/L of sodium bicarbonate at 37 ± 1 °C.** To prevent unwanted microbial growth UV rays were radiated into the solution during the experiment. Controlled additions of CO₂, using a pH probe attached to a gas dispensing apparatus, ensured that the pH of the solution was maintained at 7.4 ± 0.2 throughout immersion.

Following the completion of the test, samples were removed from the solution, rinsed with distilled water, then ethanol, and allowed to dry in air completely. Corrosion product removal was done in a hydrochloric acid and hexamethylenetetramine solution. Samples were immersed for 10 minutes, rinsed with ethanol, and ultrasonically cleaned in ethanol for 5 minutes. The cleaning cycle was repeated 5 times and plotted against the mass loss to

determine the most accurate weight change of the sample as per ASTM G1-03 [46].

Subsequently, the corrosion rate was determined using [47]:

$$CR_i = 8.71 \times 10^4 \frac{W}{At\rho} \quad (3)$$

Where W is the weight loss, A is the surface area, t is the time of exposure and ρ is the density. The surface area was calculated based on the CAD design.

2.5 Biocompatibility Assessment

2.5.1 Cell culture

MC3T3-E1 (Pre-osteoblast cell line) was obtained from American Type Culture Collection (ATCC) and cultured in Dulbecco's modified Eagle's medium (DMEM; Gibco®, Life Technologies Pty Ltd., Australia) containing 10% fetal bovine serum (FBS; In Vitro Technologies, Australia) and 1% (v/v) penicillin/streptomycin (P/S; Gibco®, Life Technologies Pty Ltd., Australia) and incubated at 37 °C in a 95% humidified atmosphere of 5% CO₂. Culture medium was changed every 2-3 days. When cultured cells reached 90% confluence, these were passaged by a 3 minutes exposure to 0.25% trypsin (containing 1mM EDTA, Gibco®, Life Technologies Pty Ltd., Australia).

2.5.2 Biocompatibility test

To evaluate the biocompatibility of the Fe-35Mn scaffolds, an indirect cytotoxicity test was performed according to ISO 10993-5:2009 [48]. To prepare extract mediums, the Fe-35Mn scaffolds were cleaned, sterilized, and incubated in Dulbecco's modified Eagle's medium (DMEM) with 10% fetal bovine serum (FBS) and 1% p/s for 72 h in a humidified atmosphere (5% CO₂) at 37 °C. The surface area of extraction medium ratio was 1.25 ml/cm². The supernatant fluid was withdrawn and centrifuged, then refrigerated at 4 °C prior to use. DMEM medium with 10% FBS and 1% p/s was used as the negative control. Cytotoxicity of the extract medium on cells was evaluated by 3-(4, 5-Dimethylthiazol-2-yl)-2, 5-diphenyltetrazolium bromide (MTT) assay.

MC3T3-E1 cells (5×10⁴) in 100 µl DMEM supplemented with 10% FBS were seeded in 96-well plates and incubated overnight. The medium was then replaced with 100 µl extracts (original or 10 times dilution) the next day. After incubating the cells in a humidified atmosphere with 5% CO₂ at 37 °C for 1 and 3 days, 10 µl of fresh MTT solution (5 mg/ml, Sigma-Aldrich Pty Ltd., Sydney, Australia) was added into each well. Cells were further incubated for 4 hours. Afterwards, the medium was carefully removed and 100 µl dimethyl sulfoxide was added into each well to solubilize the formazan product. The plate was gently shaken and protected from light for 20 minutes at room temperature, after which absorbance was read by a microplate reader (Tecan Infinite M200 PRO, Switzerland) at 570 nm. Extract medium without cells was used as control for the absorbance reading. All the results were normalized against the absorbance of blank wells. The MTT tests were repeated three times with four replications.

2.5.3 Effects of Fe-35Mn scaffolds on cell morphology

In order to observe the effect of extracts on morphometry of cells, 2.0×10^4 MC3T3-E1 cells per well were collected and seeded into 24-well culture plates. The culture medium was replaced the next day, and cell incubation of 1 and 3 days followed. After the incubation period, cells were washed carefully two times with phosphate buffered saline (PBS) solution, fixed with 4% paraformaldehyde for 20 minutes at room temperature, again washed two times, and permeabilized by 0.1% Triton X-100 for 5 minutes at room temperature.

Afterwards, the cells were mixed with 100 μ l of Alexa Fluor 488 phalloidin (Life Technologies Corporation, Australia), kept in dark incubation at 25 °C for 20 minutes, then washed thoroughly with PBS. The cells were mounted on a slide and a drop of an aqueous mounting medium, Fluoroshield™ with DAPI (Sigma-Aldrich, Australia), was added to preserve fluorescence of the cell smears. Specimens were viewed and analysed under an inverted confocal laser scanning microscope (Nikon C2+, Nikon, Japan).

2.5.4 Observation of cells growth on the iron-manganese scaffolds

The Fe-35Mn scaffolds were sterilized with 70% ethanol and placed in 24-well plates. Then 1.0×10^4 MC3T3-E1 cells were seeded on the top of the scaffolds and cultured for 1 day. After that cells were washed carefully two times with PBS solution, fixed with 4% paraformaldehyde for 20 minutes at room temperature, again washed two times, and dehydrated with a series of ethanol (70, 80, 90, 100 %). After replacing all the solution with 100% ethanol, the samples were dried with a critical point dryer (Tousimis Samdri-780 CPD

system, USA). Samples were coated with Iridium and observed with a field emission SEM (JEOL 7800, JEOL, Japan) at an operating voltage of 1-3 kV.

2.5.5 Statistical Analysis

All experiments were performed at least in triplicate independently with each one repeated for three times, and data are presented as mean \pm standard error of mean (S.E.M). Analysis was conducted using Graphpad Prism 8.0 (Graphpad software, San Diego, CA, USA). For statistical comparisons between two groups, Students' t-test was used. The statistical differences were considered significant if the P-value < 0.05 .

2.6 in vivo Assessment

2.6.1 Animal tests

The *in vivo* evaluation of the Fe-35Mn scaffolds was performed on Sprague Dawley (SD) rats using a calvarial defect model. All protocol and procedures were approved by the Ethics Committee of the University of Queensland. SD rats were housed in standard conditions (1 rat per cage at room temperature with 12 h of light/dark cycle). A total of 3 rats were included in this study. A normal diet was provided before surgery and a soft diet, consisting of liquid gel packs, as provided for the animals 2 days preoperative and 1 week postoperative, gradually changing back to a regular diet.

The calvarial defects were created surgically. First, rats were anaesthetised with an intraperitoneal injection of ketamine (75 mg/kg) and domitor (0.5 mg/Kg) with 25-27 gauge needles. Additionally, 0.25 ml of 0.4% lidocaine was injected locally with 25-27 G needles. After 5-10 minutes, the condition of animals were tested by gently squeezing the toe to check for a withdrawal reflex. Once anaesthetised, a mid-longitudinal, 15 mm skin incision was made on the dorsal surface of the cranium, care was taken to ensure that the periosteum was completely cleared from the surface of the cranial bone by scraping. A trephine bur was used to create a circular 5 mm diameter defects in the rat cranium. The full thickness (approximately 1.5-2 mm) of the cranial bone was carefully lifted and removed. The scaffolds were implanted in the defect area immediately. The mucosal flaps were closed using 4-0 polyglactin absorbable sutures. For the control group, the defect was covered by the mucosal flaps directly with suture. Animals were monitored closely following experimental completion whilst recovering from anaesthesia. Postoperative pain control included subcutaneous administration of Metacam (2 mg/kg) and Butorphanol (0.2 mg/kg) once per day for 3 days. After 4 weeks the rats were euthanized and the skulls were collected and fixed for following analysis.

2.6.2 Micro-CT analysis

The fresh fixed samples were placed in PBS in order to keep the samples moist and scanned using Micro-CT (μ CT40, Scanco Medical, Bassersdorf, Switzerland). Scanning was executed at 45 kV and 177 μ A with an isotropic voxel size of 6 μ m per slice in high-resolution mode. The scans were analysed with the scanner's software.

2.6.3 Undecalcified bone histological studies

The rat skulls were placed in cassettes, and first dehydrated with a series of ethanol solutions (70, 90 and 100 %) for 30 minutes each. The hard tissue was cut into thin samples using an EXAKT 12 step section system (EXAKT Technologies, Inc, USA). The rat skulls were subsequently infiltrated by ascending resin (HERAEUS KULZER Technovit 7200 VLC) and a series of diluted ethanol solutions (30/70%, 50/50%, 70/30%, and 100%) for one day in each concentration and then two days in 100% resin. Then the rat skulls were embedded in resin (HERAEUS KULZER Technovit 7200 VLC) and polymerized under Light Polymerization System (EXAKT 520) for 16 hours. Next, the rat skulls were mounted onto plastic slides and ground by Micro Grinding System (EXAKT 400 CS, Germany) to remove embedding resin and expose sample, followed by vacuum drying overnight at 40 °C. The exposed side was mounted (EXAKT 402) after vacuum drying, and cut into 100 µm sections. The remaining part was mounted again to be cut for the next sample. Subsequently, the sections were ground down to 10-20 µm (EXAKT 400 CS) for further staining.

The ground samples were stained by hematoxylin and eosin (H&E stain). This was achieved by dewaxing the samples with 100% xylene (Sigma-Aldrich, Australia) twice, for 10 minutes each time, and then gradual hydration with 100%, 90%, 70% ethanol and finally distilled water, twice for 5 minutes each step. Then the samples were stained by hematoxylin (Sigma-Aldrich, Australia) for 15 minutes, and the excess stain was washed using distilled water. After that, the samples were dehydrated using a series of ethanol solutions 70%, 90% and 100% for 5 minutes in each step. The specimen were then stained with eosin (Sigma-Aldrich, Australia) for a few seconds followed by washing in 100% ethanol. Lastly, the samples were immersed in xylene

for 5 minutes, mounted with DPX mounting media (Thermo Scientific, Australia), and observed under optical microscopy (Leica DMI8, Leica, Germany).

3.0 Results and Discussion

3.1 Material Characterization

Due to the high cooling rates characteristic of SLM [49], minor peaks of hexagonal close-packed (HCP) ϵ -martensite phase can be observed on the XRD spectra (Figure 2 A) of the Fe-35Mn scaffold, with the other being major face centred cubic (FCC) austenitic (γ) phase peaks. In the Fe-Mn systems with a low Mn content the γ -austenite phase is only stable at higher temperatures. As the Mn content increases the temperature at which austenite begins to form and is stable (austenite start (A_s) temperature) decreases [50]. The ϵ -martensite phase formation is dictated by the martensite start temperature (M_s), which also increases with increasing Mn content [50, 51]. At a certain Mn concentration the A_s and M_s reach a critical temperature for antiferromagnetic ordering, known as the Néel temperature (T_N). Past this critical temperature the γ -austenite phase is stabilised over the ϵ -martensite phase due to the paramagnetic to antiferromagnetic transformation [52]. In Fe-Mn alloys with a Mn content greater than 27 wt%, the stabilisation of the γ -austenite is so highly favoured over the ϵ -martensite phase that typically not detected except in cases where the cooling rates are very high as is the case with SLM [50]. As a consequence, only minor HCP ϵ -martensite peaks are observed in Figure 2 A.

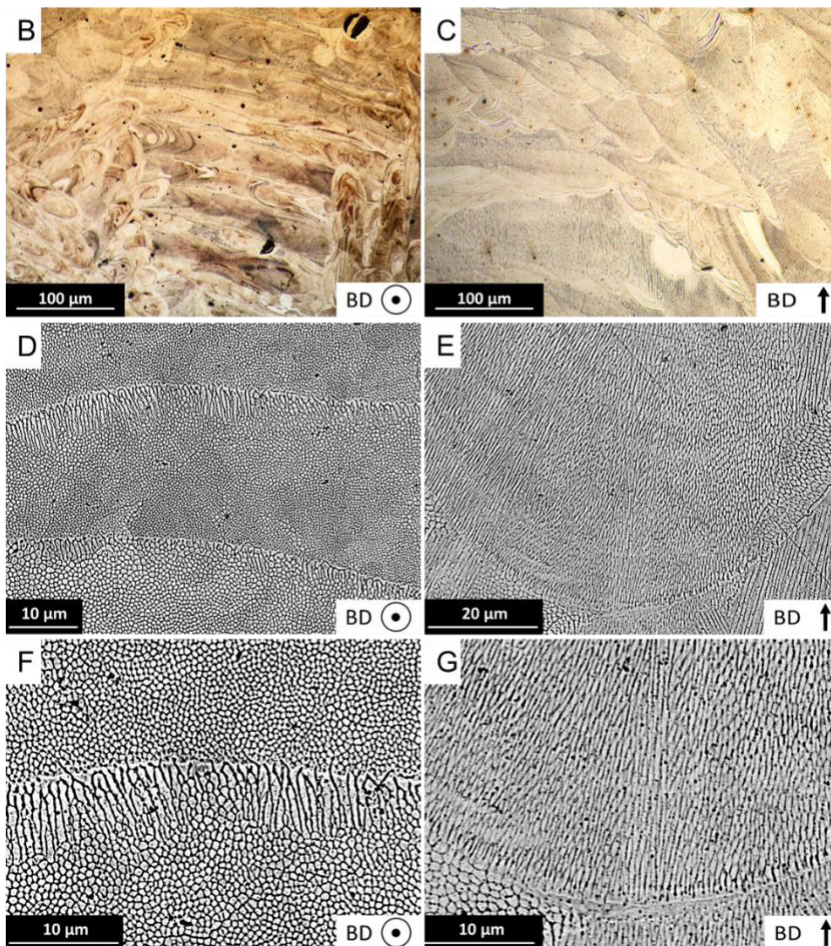
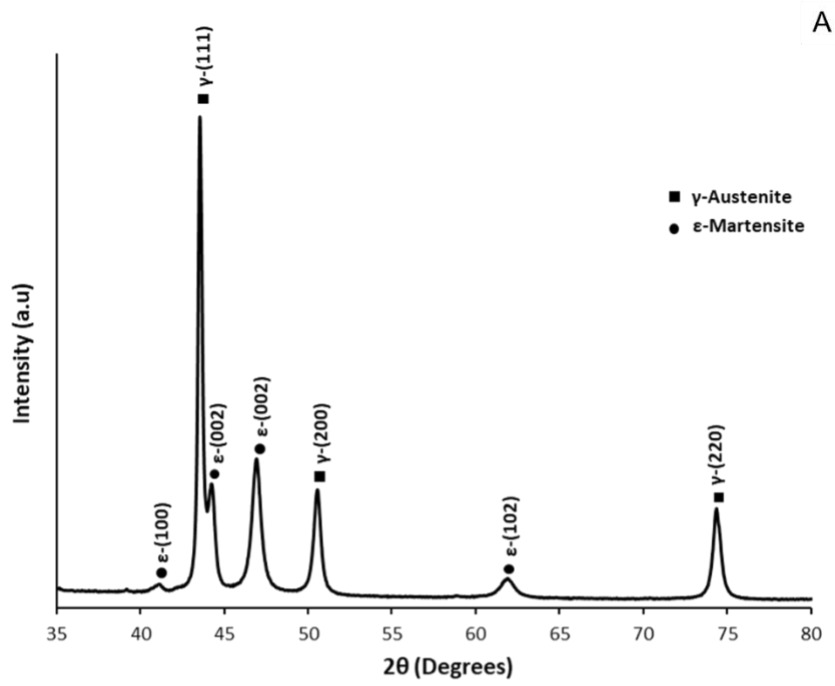


Figure 2 (A) XRD spectra of Fe-35Mn scaffold. Cross-sectional micrographs showing the melt pool outlines with build direction (BD) out of plane (B) and BD in plane (C). SEM images showing the microstructure of the Fe-35Mn scaffold with BD out of plane (D, F) and BD in plane (E, G). Please note a difference in scale bars between the microstructures to better show the features

The microstructure of the Fe-35Mn scaffold primarily consists of several large columnar austenite (γ) grains, with each grain consisting of a network of small cells as can be seen in Figure 2 D-G. Carluccio et al. postulated that cellular solidification mode dominates over dendritic solidification due to the high solidification rates typical of SLM [40]. Individual melt tracks are readily discerned due to variations in the solidified microstructure, such as cell size, which occurs dynamically throughout the melt pool as solidification conditions change. Other research has shown that key solidification parameters such as temperature gradient, interface growth rate and cooling rate change within each layer as it solidifies (i.e., conditions at the bottom of each melt pool differ from the top) [53, 54]. The microstructures observed in Figure 2 are finer than those of traditional manufacturing methods [39] because the small melt pools and high cooling rates that typically occur during SLM promote fine-grained structures. The cell size, λ , (and secondary dendrite arm spacing) is related to the cooling rate and empirical relationships have been determined. For austenitic stainless steels the relationship between cooling rate and cellular spacing has been determined by the equation [55]:

$$\lambda_1 = 80\dot{T}^{-0.33} \quad (4)$$

Where λ_1 is the primary cellular spacing and \dot{T} is the cooling rate.

The cell size in the SLM Fe-35Mn alloys is approximately $0.56 \pm 0.2 \mu\text{m}$, which according to equation 4, corresponds to a cooling rate in the range of 10^7 K/s . The lower energy density

used to achieve fine struts means that the cooling rate is on the higher end of the cooling rates typical of SLM ($10^3 - 10^8$ K/s) [56]. Furthermore, the complex heat inputs and subsequent cooling rates from the SLM scan strategies used to manufacture the scaffolds produces a multifaceted collection of direction changing columnar γ grains. From Figure 2 E some epitaxial growth on grains that are oriented favourably can be observed, resulting in grains that span across several melt pools.

For load-bearing scaffolds, the compressive strength of the scaffold should be equal to or greater than that of human cortical bone to allow for proper healing and subsequent load-transfer as the scaffold degrades. Similarly, the Young's modulus of the scaffold should be as close as possible to that of bone to prevent stress shielding [12]. Using these criteria, from Table 3 it can be seen that the SLM manufactured Fe-35Mn scaffold displays suitable mechanical properties, especially for highly loaded bone scaffold applications such as the mandible; as the mandible bone has been shown to have higher compressive strength compared to the bone in other areas [57]. The ductility should be sufficient to prevent premature failure of the scaffold. From Figure 3, it can be seen that the scaffold has a high ductility, due to a predominantly FCC γ -austenite microstructure as discussed above.

Table 3 Comparison of compression properties of SLM produced Fe-35Mn scaffolds with other biodegradable metals and human bone

Material	Young's Modulus (GPa)	0.2% Offset Yield Point (MPa)	Compressive strength at 20% Strain (MPa)
SLM Fe-35Mn Scaffold-	33.5 ± 1.7	89.2 ± 1.9	304.0 ± 7.4
Cast Fe-35Mn [58]	-	240	440+

Porous PM Fe-35Mn	15	64	567 [^]
[30]			
Cast Pure Fe [59]	203	157	498
SLM Pure Fe [59]	200	421	760
SLM Pure Fe	1.8	24	35
Scaffold [39]			
Cast Pure Mg [60]	30-40	20-30	100-180 ⁺
Cast Pure Zn [61]	100	95	200
SLM Pure Zn [62]	23	114	134 ⁺
Human Cortical	1-35 [*]	1-20 [*]	103-140 ^{*+}
Bone [63-66]			

~ Current work

* The mechanical properties of bone can vary greatly depending on the age, type of bone and health of the bone

[^] Compressive Strength at 30% strain

⁺ Ultimate compressive strength (% strain not given)

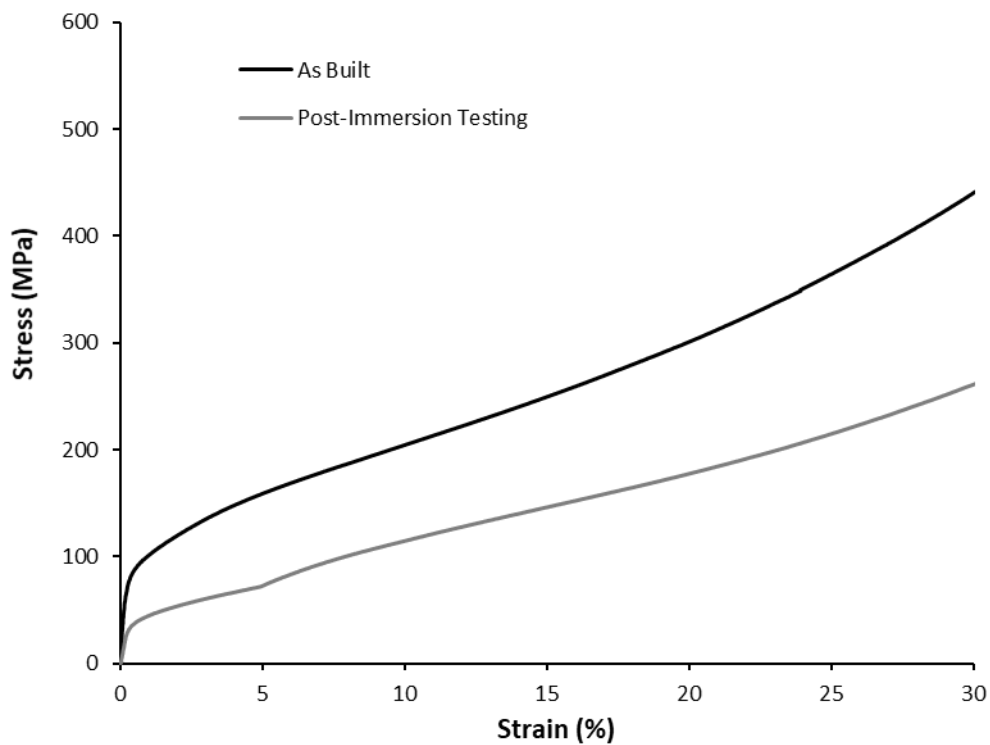


Figure 3 Compression curve of Fe-35Mn Scaffold as built and after 28 days immersion

3.2 Electrochemical and Immersion Testing

Compared to cast and SLM-manufactured pure Fe, the SLM manufactured Fe-35Mn scaffold had a higher corrosion rate (Figure 4). While it can often be abstruse to directly compare potentiodynamic polarization (PDP) results of different studies, since they are significantly influenced by experimental parameters [67], the PDP results of the cast and SLM-manufactured pure Fe [59], were measured under the same circumstances as this paper. Since the effective surface area exposed was only that of the surface (as the pores were filled), it can be quantitatively observed that the addition of Mn increases the corrosion rate, in agreement with the literature [30, 31]. The addition of 35 wt% Mn increases the susceptibility of the alloy to corrosion by lowering the standard potential of the alloy, and increasing the thermodynamic activity of the alloy in SBF [30, 31]. It is also possible that Mn-rich areas in the microstructure can lead to a higher degradation rate via enhanced localized microgalvanic corrosion.

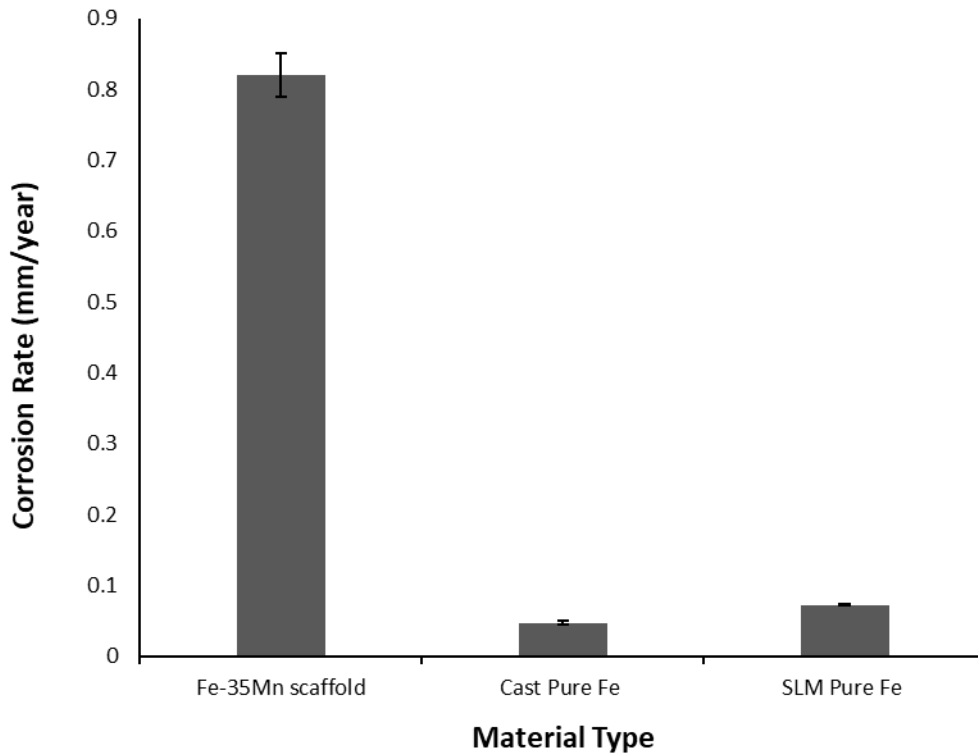


Figure 4 Potentiodynamic polarization test corrosion rate of Fe-35Mn scaffold and pure Fe (from [59])

The overall shape of the Nyquist plot in Figure 5 A is consistent with literature [30] and consist of three time constants; a low-frequency inductive loop, a large medium-frequency capacitance loop and a smaller high-frequency capacitance loop. The low frequency inductive response is likely related to the adsorption of ions on the working electrode surface [68]. The large medium-frequency capacitance loop is typical of Fe-based materials tested in SBF [30, 59]. Pure Fe (both cast and SLM manufactured) does not display the small high-frequency capacitance loop [59] that is observed in Figure 5 A. It is believed that this is caused by the presence of a porous oxide layer typical of Fe-35Mn alloys tested in SBF [30].

Figure 5 C shows the equivalent circuit used to model the EIS data and consists of Randles circuit to describe the reactions occurring at the metal-liquid interface where: R_s represents the resistance of the Hank's solution, CPE_{dl} represents the double layer capacitance and R_{ct}

the resistance to charge transfer. The secondary circuit represents the oxide layer and consist of CPE_{ox} that is associated with the oxide layer capacitance, R_{ox} is the resistance of the oxide layer, and L is associated with the inductive response of the oxide layer. The use of constant phase elements (CPE) models non-ideal dielectric behaviour possibly caused by non-uniform coatings, dislocations, impurities, and other defects. The CPEs are defined by Q (the CPE value) and n (the CPE exponent). As seen in Table 4, the CPE exponents both fall between 0.65-0.85 and thus the CPEs represent a dielectric relaxation time in frequency space [69].

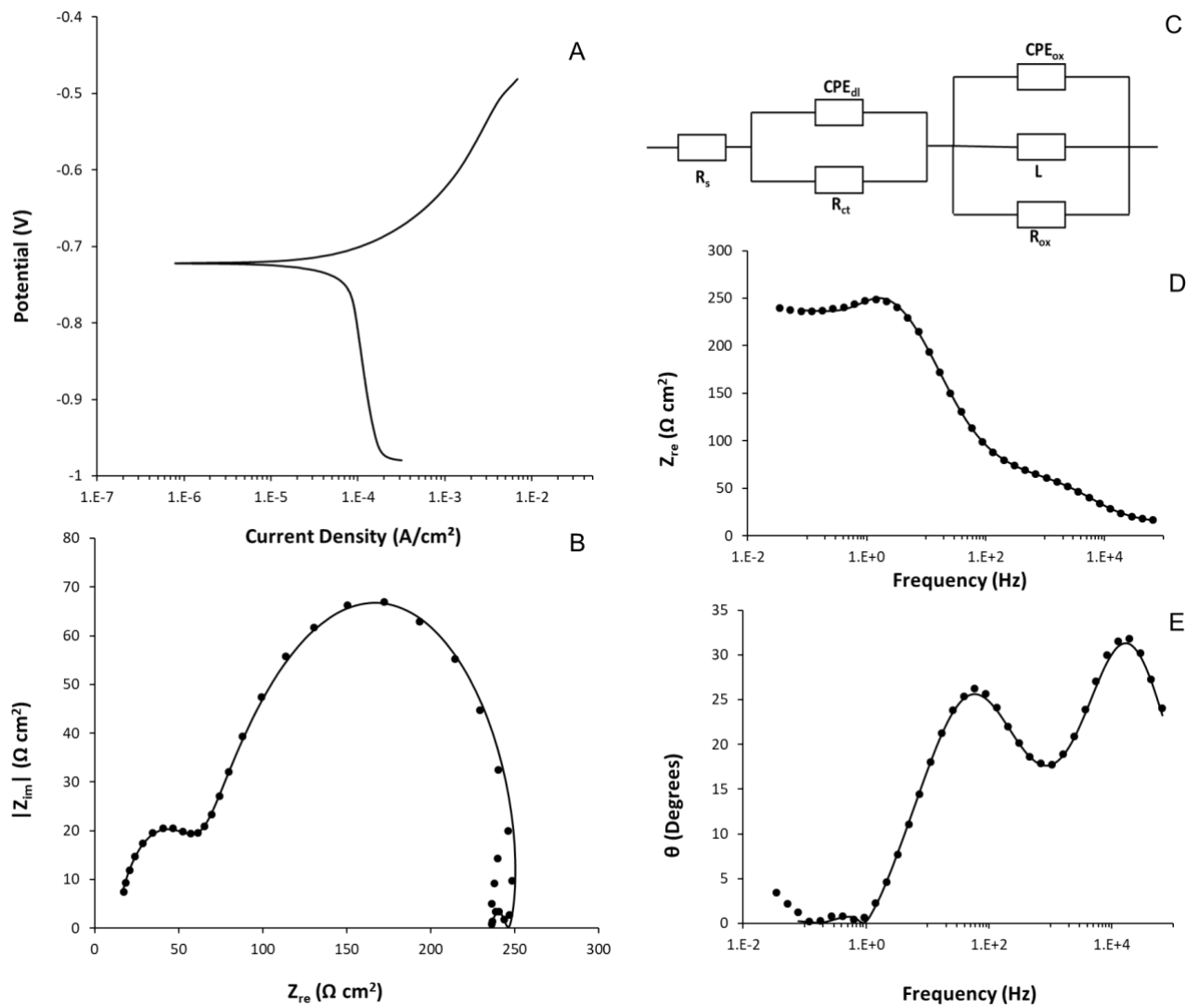


Figure 5 (A) Polarization curve of SLM manufactured Fe-35Mn scaffold, (C) EIS data fitted with proposed equivalent circuit models; (B) Nyquist plot, (D) Bode plot, Z_{re} vs frequency, (E) Bode plot, phase angle vs frequency

Table 4 EIS circuit parameters of Fe-35Mn scaffold

	i_{corr} ($\mu\text{A}/\text{cm}^2$)	R_s ($\Omega \text{ cm}^2$)	Q_{dl} ($\mu\text{S}\cdot\text{Sn}/\text{cm}^2$)	n_{dl}	R_{ct} ($\Omega \text{ cm}^2$)	Q_{ox} ($\mu\text{S}\cdot\text{Sn}/\text{cm}^2$)	n_{ox}	L ($\Omega\cdot\text{s}\cdot\text{cm}^2$)	R_{ox} ($\Omega \text{ cm}^2$)
Fe-35Mn	68.5 ± 2.1	14.3 ± 2.7	1747 ± 100	0.69 ± 0.01	228 ± 5.1	48.5 ± 14.5	0.80 ± 0.05	6.9 ± 0.5	45.6 ± 3.6

Compared to pure Fe immersion tested under similar conditions that had a corrosion rate of 0.062 mm/year [30], the Fe-35Mn scaffold had a much higher corrosion rate of 0.42 ± 0.03 mm/year. This is attributed to a combination of the effect of the manufacturing method, the effect of the addition of Mn and the design of the scaffold, all of which can increase the corrosion rate. Using SLM, a hierarchical porous architecture was achieved, and so more of the surface area of the metal is exposed to the environment [70], and thus increases the degradation rate. Furthermore, the high cooling rates and the complex heat inputs typical of SLM impart high levels of internal defects, dislocations and residual stresses [37] into the scaffold. This can cause local destabilisation of the passive film [71], creating small cathodic sites resulting in localised corrosion and thus an overall increased corrosion rate [59].

Previous studies have shown that additions of Mn can further change the dielectric behaviour of the oxide layer due to the structural mismatch between Fe and Mn oxide films, allowing for greater transport through the oxide layer and thus increasing the surface corrosion rate [30].

Different degradation patterns were observed on different parts of the scaffold; on the outer surface corrosion patterns were relatively unvarying (Figure 6 A-B), but on the inner surface, degradation behaviour was different on the periphery when compared to the centre (Figure 6 C-D). Outer-surface pores surface are initially likely to be highly susceptible to corrosion due

to differential aeration cells that form due to an oxygen concentration difference inside and outside the scaffold. Furthermore, the inside of the pores has a larger exposed surface as it was not polished when compared to the rest of the surface. These phenomena can lead to localised alkalization [14] and as the degradation proceeds, calcium-phosphate apatites form in the pores as shown by the high content of Ca and P in Figure 6 A. Degradation on the rest of the external surface is characterised by the presence of Fe-oxide and Mn-oxide with small amounts of Ca and P (Figure 6 B).

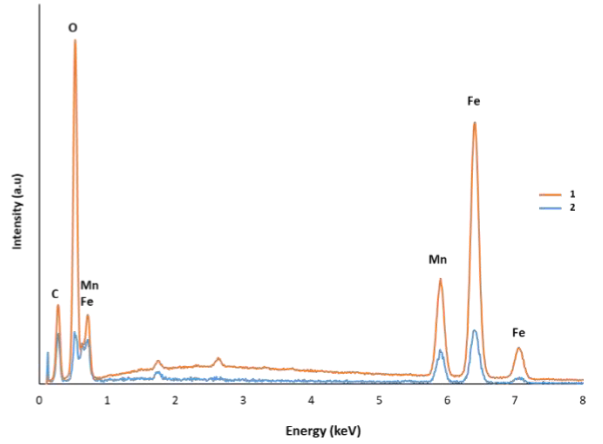
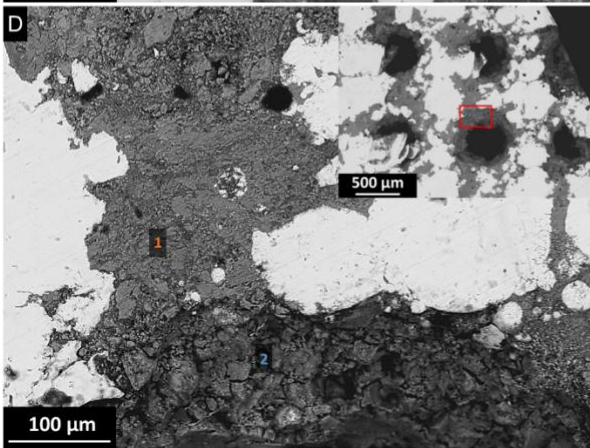
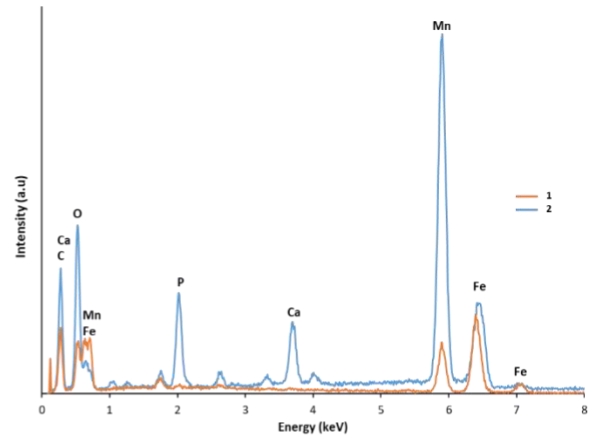
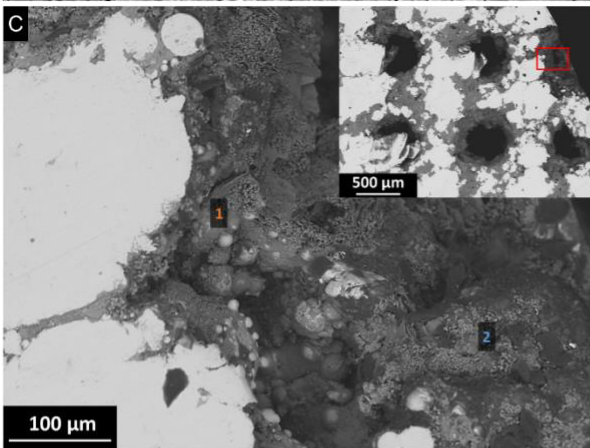
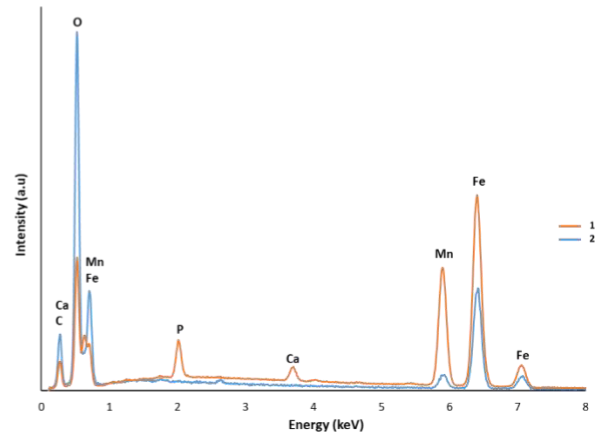
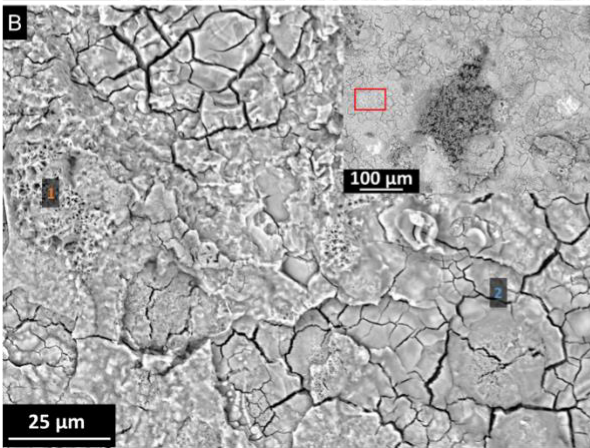
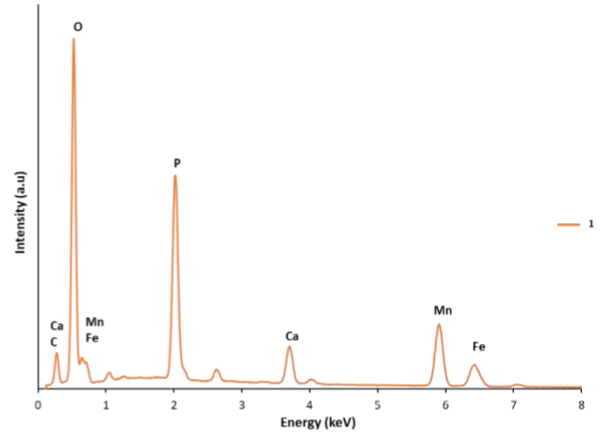
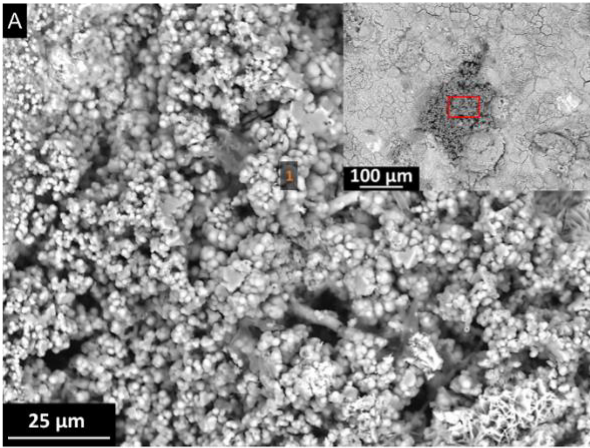


Figure 6 SEM and EDS analysis SLM manufactured Fe-35Mn scaffold showing corrosion product in the outer surface pore (A), and on the surface (B), the inner surface on the edge (C), and at the centre of the scaffold (D)

Degradation patterns on the periphery of the inner surface showed a high amount of Ca, P and Mn, likely forming Mn phosphates and calcium-phosphate apatites (Figure 6 C). On the other hand, corrosion in the centre of the inner surface of the scaffold, occurred at the thinnest parts of the struts between pores. As shown in Figure 6 D the degradation product mainly consists of Fe and Mn oxides.

Significant degradation of the outer surface, as characterised by the crater-like landscape seen in Figure 8 A-B, can be observed subsequent to the removal of the corrosion product. On the inner surface, however, significant corrosion in and around the pores can be seen along with intra-strut corrosion seen in Figure 8 C leading to the canyon-like cavities observed in Figure 8 D. This type of localised corrosion is generally not desired as it can lead to premature failure of the implant, rather the more uniform corrosion as observed on the outer surface is preferred. From Figure 3 it can be observed that the degradation did reduce the overall bulk yield strength of the scaffold, but the randomised local strut failure did not decrease the ductility of the scaffold, nor induce irregular behaviour during compression. The localised corrosion is expected to improve the overall implant degradation rate [39]. Additionally, during healing, there is a stress transfer from the scaffold into the healing bone, which further decreases the effects of localised degradation on the mechanical properties of the scaffold. This indicates that the possible loss of mechanical strength of the porous implant due to corrosion is not really a concern and that the beneficial effects of pores on the corrosion rate should now come to focus. The biodegradation rate of biodegradable Fe is often deemed too slow, therefore increasing the biodegradation rate is critically the more important issue [72].

If not, the implant can behave akin to a permanent metal and invoke foreign body reactions leading to implant loosening and rejection [14]. For bone scaffolds there is not an ideal corrosion rate, rather there is an ideal performance of the scaffold as can be seen from Figure 7. The scaffold should retain sufficient mechanical properties to prevent premature stress transfer to the newly forming bone, before slowly transferring the load to the bone after sufficient time; having completed its purpose the mechanical integrity is no longer a prerequisite and the scaffold can then degrade away entirely.

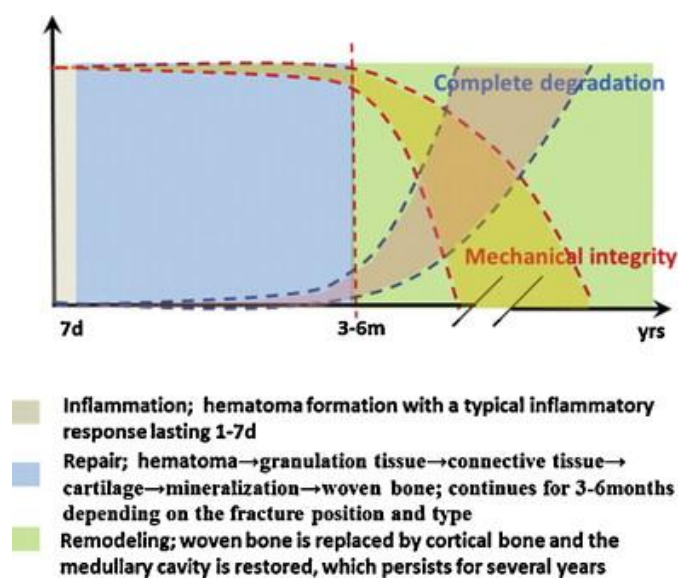


Figure 7 Relationship between mechanical integrity and degradation rate of bone scaffold during the healing process. Reproduced with permission from [14].

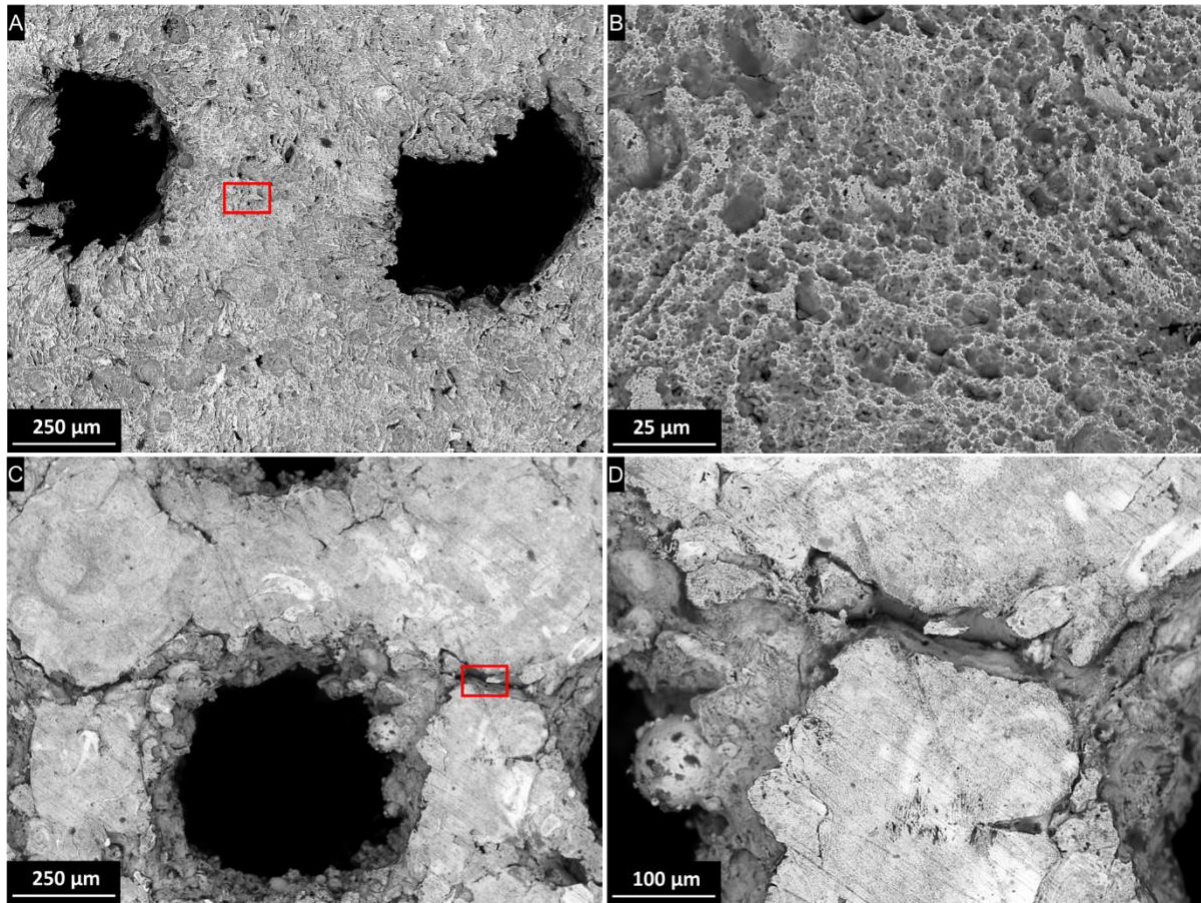


Figure 8 Different magnification SEM images after corrosion product removal of the outer surface (A, B) and inner surface (C, D)

3.3 Biological Characterisation

3.3.1 Biocompatibility of Fe-35Mn scaffold

The effect of the Fe-35Mn on cell proliferation was evaluated by culturing murine preosteoblast cells (MC3T3-E1) with Fe-35Mn scaffold extract medium. As shown in Figure 9 A-D, cells growth was significant, and cell density increased along with time. Quantitative data showed there was not a difference in the cell density between the Fe-35Mn scaffold group and control group (cells in normal culture medium) (Figure 9 E), indicating that the proliferation rates were not affected. The metabolic activity of MC3T3-E1 after incubation with the Fe-35Mn scaffold

extraction was also measured using MTT assay. As shown in Figure 9 F, the Fe-35Mn alloy exhibited very good cell viability towards mammalian cells. The average values of cell viability after 1 and 3 days incubation with the Fe-35Mn showed no statistically significant difference compared to the control group ($p > 0.05$). These results indicated that the Fe-35Mn scaffold has good biocompatibility, which is consistent with literature reports of Fe-Mn alloys [30, 73].

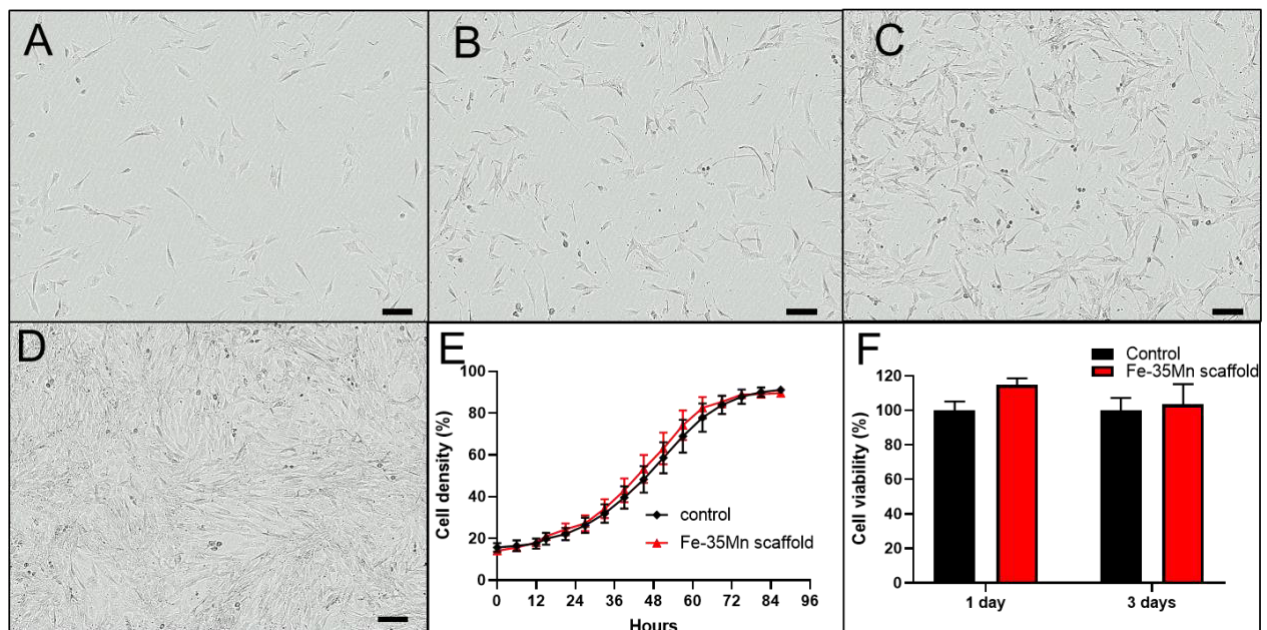


Figure 9 The effects of the Fe-35Mn scaffold extraction on cell proliferation and viability. (A-D) images of cells cultured at the Fe-35Mn scaffold extraction medium at a time of 0, 24, 48, and 72 hours, respectively. (E) cell density, (F) cell viability by MTT test. Scale bar in A-D: 50 μm. Data represented as Mean ± S.E.M. from n=3 independent experiments.

3.3.2 Cell morphology

The effect of extracts on cell morphology was also examined. The cytoskeletons of MC3T3-E1 were stained using FITC-phalloidin, which exhibits a high affinity to actin filaments, while the nuclei were stained with DAPI. Results showed that the cell morphology was elongated, which is typical of fibroblastic mammalian cells. The morphology of cells cultured with Fe-

35Mn scaffold extraction was similar to the untreated control after 1 and 3 days incubation, as shown in Figure 10.

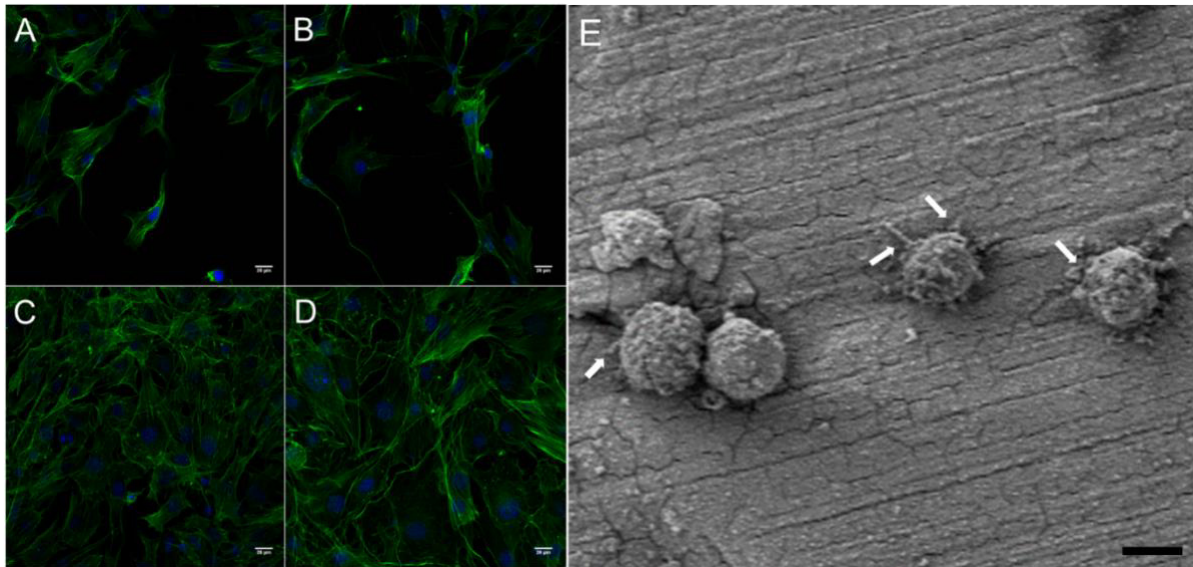


Figure 10 Cell morphology of cells after being co-cultured without (A, C) or with (B, D) Fe-35Mn scaffold extract for 1 (A, B) and 3 days (C, D). (E) SEM image of MC3T3-E1 on the surface of the Fe-35Mn scaffold. The filopodia are indicated by white arrows. Scale bar in A-E: 20 μm .

The morphology of MC3T3-E1 cells on the surfaces of the Fe-35Mn scaffold samples were also observed with SEM after cells were placed on the scaffold surface for 4 hours. As shown in Figure 10 E, some cells were found to adhere to the surface of scaffold and it is noted that filopodia (indicated by white arrows) were formed and attached to the scaffold. Filopodia are thin membrane protrusions and necessary for cell migration and adhesion [74]. The presence of filopodia on the Fe-35Mn scaffold indicates that the alloy is suitable for osteoblast adhesion [75].

3.3.3 Evaluation of the osteointegration of SLM-manufactured Fe-35Mn alloy in vivo

The initial healing phase of the CBD is critically important in determining both the short and long-term success of the implant. The implant-to-bone contact area of the Fe-35Mn scaffold was observed using histological analysis. Newly formed bone matrix was observed in direct contact with the implant surface after 4 weeks (Figure 11 A). Osteoid and osteoblasts were also found in the newly formed bone layers, which indicated the ongoing bone-forming process. This shows osteointegration into the Fe-35Mn scaffold; where the bone regeneration process started in the defect area followed by bone apposition on the scaffold. Micro-CT was used to observe the new bone formation in the bone defect area and the scaffold (Figure 11 B-E). From the series of images from the middle to the top of the implant, the Fe-35Mn scaffold closely bonded to the bone tissue with no observable gaps. The porous nature of the scaffold can be also seen.

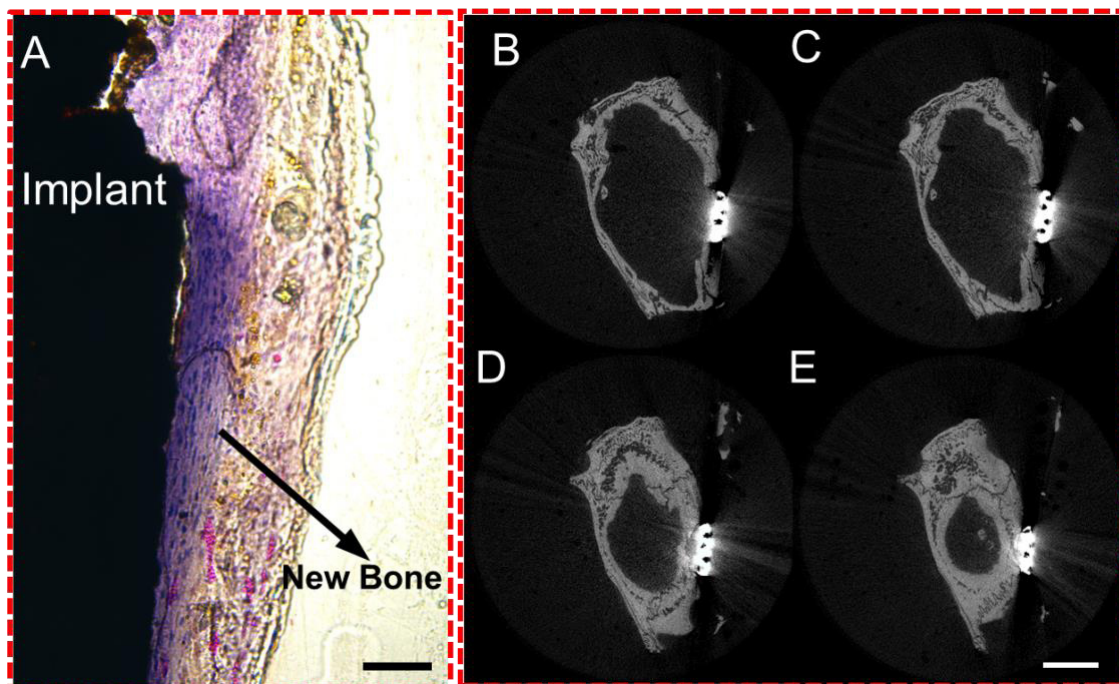


Figure 11 In vivo evaluation of osteointegration of Fe-35Mn scaffold after implantation in the rat cranial bone defect for 4 weeks. (A) Histological image of the implant in bone and new bone formation on the surface of implant. (B-E) Series of images from micro-CT analysis of the bone defect with Fe-35Mn scaffold, from bottom (B) to top (E). *Scale bar in A: 50 μ m. Scale bar in B-E: 5 mm.*

4.0 Conclusion

This study investigated the feasibility and performance of Fe-35Mn bone scaffolds manufactured using SLM. After in-depth characterisation, it was shown that the SLM-manufactured Fe-35Mn implants show great potential for future biodegradable bone scaffolds for load-bearing applications. The results of the study can be summarised as follows:

- Despite the high cooling rate typical of SLM, the microstructure consisted primarily of FCC γ -austenite, leading to **high** ductility of the scaffold.
- **The presence of calcium-based corrosion products, such as calcium-phosphate apatites, at the surface limited the amount of dissolved oxygen reaching the metal and, consequently, reduced corrosion rates. However, the corrosion rate was still much higher than that of bulk pure Fe owing to a synergistic combination of the manufacturing method, the addition of Mn and the design of the scaffold.**
- The mechanical properties of the Fe-35Mn scaffold were sufficient for load-bearing applications even after 28 days immersion.
- The scaffold displayed **biocompatibility comparable to the control and a high** viability towards mammalian cells. Furthermore, filopodia attachment to the scaffold shows that the scaffold displays *in vitro* osteoblast adhesion.
- The reported *in vivo* study, which is the first to be reported for an SLM-manufactured Fe-based scaffold, showed that the implant successfully integrated with the original bone, and even stimulated bone formation after only 4 weeks of implantation.

Acknowledgements

DC, MJB, DK, JV and MSD acknowledge the support of the School of Mechanical and Mining Engineering, the Queensland Centre for Advanced Materials processing and Manufacturing and the Australian Research Council Research Hub for Advanced Manufacturing of Medical Devices (IH150100024). CX acknowledges the support of National Health & Medical Research Council of Australia (NHMRC) Early Career Fellowship. AGD, and BP acknowledge the support of European Union, Repubblica Italiana, Regione Lombardia and FESR for the project MADE4LO under the call "POR FESR 2014-2020 ASSE I - AZIONE I.1.B.1.3". MJB also acknowledges the support of the Australian Research Council Discovery Program and is in receipt of Discover Early Career Researcher Award (DE160100260). The authors would like to thank Dr. Karine Mardon from the Queensland Node of the National Imaging Facility, located at the Centre for Advanced Imaging at the University of Queensland

Table of Figures

Figure 1 (A) CAD of scaffold, (B) Repeating unit cell, (C) As manufactured scaffold.....	9
Figure 2 (A) XRD spectra of Fe-35Mn scaffold. Cross-sectional micrographs showing the melt pool outlines with build direction (BD) out of plane (B) and BD in plane (C). SEM images showing the microstructure of the Fe-35Mn scaffold with BD out of plane (D, F) and BD in plane (E, G). Please note a difference in scale bars between the microstructures to better show the features	22
Figure 3 Compression curve of Fe-35Mn Scaffold as built and after 28 days immersion	25
Figure 4 Potentiodynamic polarization test corrosion rate of Fe-35Mn scaffold and pure Fe (from [59])	27
Figure 5 (A) Polarization curve of SLM manufactured Fe-35Mn scaffold, (C) EIS data fitted with proposed equivalent circuit models; (B) Nyquist plot, (D) Bode plot, Z_{re} vs frequency, (E) Bode plot, phase angle vs frequency	28
Figure 6 SEM and EDS analysis SLM manufactured Fe-35Mn scaffold showing corrosion product in the outer surface pore (A), and on the surface (B), the inner surface on the edge (C), and at the centre of the scaffold (D)	32
Figure 7 Relationship between mechanical integrity and degradation rate of bone scaffold during the healing process. Reproduced with permission from [14].	33
Figure 8 Different magnification SEM images after corrosion product removal of the outer surface (A, B) and inner surface (C, D)	34
Figure 9 The effects of the Fe-35Mn scaffold extraction on cell proliferation and viability. (A-D) images of cells cultured at the Fe-35Mn scaffold extraction medium at a time of 0, 24, 48, and 72 hours, respectively. (E) cell density, (F) cell viability by MTT test. Scale bar in A-D: 50 μ m. Data represented as Mean \pm S.E.M. from n=3 independent experiments.	35

Figure 10 Cell morphology of cells after being co-cultured without (A, C) or with (B, D) Fe-35Mn scaffold extract for 1 (A, B) and 3 days (C, D). (E) SEM image of MC3T3-E1 on the surface of the Fe-35Mn scaffold. The filopodia are indicated by white arrows. Scale bar in A-E: 20 μm	36
Figure 11 In vivo evaluation of osteointegration of Fe-35Mn scaffold after implantation in the rat cranial bone defect for 4 weeks. (A) Histological image of the implant in bone and new bone formation on the surface of implant. (B-E) Series of images from micro-CT analysis of the bone defect with Fe-35Mn scaffold, from bottom (B) to top (E). Scale bar in A: 50 μm . Scale bar in B-E: 5 mm.	37
Table 1 Percentage Porosity of Fe-35Mn Scaffold.....	11
Table 2 Chemical composition of scaffold.	12
Table 3 Comparison of compression properties of SLM produced Fe-35Mn scaffolds with other biodegradable metals and human bone.....	24
Table 4 EIS circuit parameters of Fe-35Mn scaffold.....	29

References

- [1] N.M. Haines, W.D. Lack, R.B. Seymour, M.J. Bosse, Defining the Lower Limit of a "Critical Bone Defect" in Open Diaphyseal Tibial Fractures, *Journal of orthopaedic trauma* 30(5) (2016) e158-63.
- [2] M. Navarro, A. Michiardi, O. Castaño, J.A. Planell, Biomaterials in orthopaedics, *Journal of the Royal Society Interface* 5(27) (2008) 1137-1158.
- [3] L. Roseti, V. Parisi, M. Petretta, C. Cavallo, G. Desando, I. Bartolotti, B. Grigolo, Scaffolds for Bone Tissue Engineering: State of the art and new perspectives, *Materials Science and Engineering: C* 78 (2017) 1246-1262.
- [4] D.F. Williams, On the mechanisms of biocompatibility, *Biomaterials* 29(20) (2008) 2941-2953.
- [5] S. Bose, M. Roy, A. Bandyopadhyay, Recent advances in bone tissue engineering scaffolds, *Trends in Biotechnology* 30(10) (2012) 546-554.
- [6] D.W. Hutmacher, Scaffolds in tissue engineering bone and cartilage, *Biomaterials* 21(24) (2000) 2529-2543.
- [7] Y. Liu, J. Lim, S.-H. Teoh, Review: Development of clinically relevant scaffolds for vascularised bone tissue engineering, *Biotechnology Advances* 31(5) (2013) 688-705.
- [8] S. Yang, J. Wang, L. Tang, H. Ao, H. Tan, T. Tang, C. Liu, Mesoporous bioactive glass doped-poly (3-hydroxybutyrate-co-3-hydroxyhexanoate) composite scaffolds with 3-dimensionally hierarchical pore networks for bone regeneration, *Colloids and surfaces. B, Biointerfaces* 116 (2014) 72-80.
- [9] J.D. Bobyn, G.J. Stackpool, S.A. Hacking, M. Tanzer, J.J. Krygier, Characteristics of bone ingrowth and interface mechanics of a new porous tantalum biomaterial, *The Journal of bone and joint surgery. British volume* 81(5) (1999) 907-14.
- [10] F.A. Shah, O. Omar, F. Suska, A. Snis, A. Matic, L. Emanuelsson, B. Norlindh, J. Lausmaa, P. Thomsen, A. Palmquist, Long-term osseointegration of 3D printed CoCr constructs with an interconnected open-pore architecture prepared by electron beam melting, *Acta Biomaterialia* 36 (2016) 296-309.
- [11] S. Van Bael, Y.C. Chai, S. Truscello, M. Moesen, G. Kerckhofs, H. Van Oosterwyck, J.P. Kruth, J. Schrooten, The effect of pore geometry on the in vitro biological behavior of human periosteum-derived cells seeded on selective laser-melted Ti6Al4V bone scaffolds, *Acta Biomaterialia* 8(7) (2012) 2824-2834.
- [12] M. Geetha, A.K. Singh, R. Asokamani, A.K. Gogia, Ti based biomaterials, the ultimate choice for orthopaedic implants – A review, *Progress in Materials Science* 54(3) (2009) 397-425.
- [13] Y. Okazaki, E. Gotoh, Comparison of metal release from various metallic biomaterials in vitro, *Biomaterials* 26(1) (2005) 11-21.
- [14] Y.F. Zheng, X.N. Gu, F. Witte, Biodegradable metals, *Materials Science and Engineering: R: Reports* 77 (2014) 1-34.
- [15] H. Li, Y. Zheng, L. Qin, Progress of biodegradable metals, *Progress in Natural Science: Materials International* 24(5) (2014) 414-422.
- [16] W. Maret, The Metals in the Biological Periodic System of the Elements: Concepts and Conjectures, *International journal of molecular sciences* 17(1) (2016).
- [17] M.P. Staiger, A.M. Pietak, J. Huadmai, G. Dias, Magnesium and its alloys as orthopedic biomaterials: A review, *Biomaterials* 27(9) (2006) 1728-1734.
- [18] F. Witte, V. Kaese, H. Haferkamp, E. Switzer, A. Meyer-Lindenberg, C.J. Wirth, H. Windhagen, In vivo corrosion of four magnesium alloys and the associated bone response, *Biomaterials* 26(17) (2005) 3557-3563.
- [19] M.G. Seelig, A study of magnesium wire as an absorbable suture and ligature material, *Archives of Surgery* 8(2) (1924) 669-680.
- [20] H. Windhagen, K. Radtke, A. Weizbauer, J. Diekmann, Y. Noll, U. Kreimeyer, R. Schavan, C. Stukenborg-Colsman, H. Waizy, Biodegradable magnesium-based screw clinically equivalent to

- titanium screw in hallux valgus surgery: short term results of the first prospective, randomized, controlled clinical pilot study, *BioMedical Engineering OnLine* 12(1) (2013) 62.
- [21] Y. Li, J. Zhou, P. Pavanram, M.A. Leeflang, L.I. Fockaert, B. Pouran, N. Tümer, K.U. Schröder, J.M.C. Mol, H. Weinans, H. Jahr, A.A. Zadpoor, Additively manufactured biodegradable porous magnesium, *Acta Biomaterialia* 67 (2018) 378-392.
- [22] T. Kraus, S.F. Fischerauer, A.C. Hänzi, P.J. Uggowitzer, J.F. Löffler, A.M. Weinberg, Magnesium alloys for temporary implants in osteosynthesis: In vivo studies of their degradation and interaction with bone, *Acta Biomaterialia* 8(3) (2012) 1230-1238.
- [23] P.K. Bowen, J. Drelich, J. Goldman, Zinc Exhibits Ideal Physiological Corrosion Behavior for Bioabsorbable Stents, *Advanced Materials* 25(18) (2013) 2577-2582.
- [24] J. Venezuela, M.S. Dargusch, The influence of alloying and fabrication techniques on the mechanical properties, biodegradability and biocompatibility of zinc: A comprehensive review, *Acta Biomaterialia* 87 (2019) 1-40.
- [25] J. Čapek, E. Jablonská, J. Lipov, T.F. Kubatík, D. Vojtěch, Preparation and characterization of porous zinc prepared by spark plasma sintering as a material for biodegradable scaffolds, *Mater. Chem. Phys.* 203 (2018) 249-258.
- [26] Y. Hou, G. Jia, R. Yue, C. Chen, J. Pei, H. Zhang, H. Huang, M. Xiong, G. Yuan, Synthesis of biodegradable Zn-based scaffolds using NaCl templates: Relationship between porosity, compressive properties and degradation behavior, *Mater. Charact.* 137 (2018) 162-169.
- [27] H. Hermawan, D. Dubé, D. Mantovani, Degradable metallic biomaterials: Design and development of Fe–Mn alloys for stents, *Journal of Biomedical Materials Research Part A* 93A(1) (2010) 1-11.
- [28] H.K. Lim, J.L. Riddell, A.C. Nowson, O.A. Booth, A.E. Szymlek-Gay, Iron and Zinc Nutrition in the Economically-Developed World: A Review, *Nutrients* 5(8) (2013).
- [29] M. Peuster, P. Wohlsein, M. Brüggmann, M. Ehlerding, K. Seidler, C. Fink, H. Brauer, A. Fischer, G. Hausdorf, A novel approach to temporary stenting: degradable cardiovascular stents produced from corrodible metal—results 6–18 months after implantation into New Zealand white rabbits, *Heart* 86(5) (2001) 563.
- [30] M.S. Dargusch, A. Dehghan-Manshadi, M. Shahbazi, J. Venezuela, X. Tran, J. Song, N. Liu, C. Xu, Q. Ye, C. Wen, Exploring the Role of Manganese on the Microstructure, Mechanical Properties, Biodegradability, and Biocompatibility of Porous Iron-Based Scaffolds, *ACS Biomaterials Science & Engineering* 5(4) (2019) 1686-1702.
- [31] M. Schinhammer, A.C. Hänzi, J.F. Löffler, P.J. Uggowitzer, Design strategy for biodegradable Fe-based alloys for medical applications, *Acta Biomaterialia* 6(5) (2010) 1705-1713.
- [32] H. Hermawan, A. Purnama, D. Dube, J. Couet, D. Mantovani, Fe-Mn alloys for metallic biodegradable stents: degradation and cell viability studies, *Acta biomaterialia* 6(5) (2010) 1852-60.
- [33] X. Wang, S. Xu, S. Zhou, W. Xu, M. Leary, P. Choong, M. Qian, M. Brandt, Y.M. Xie, Topological design and additive manufacturing of porous metals for bone scaffolds and orthopaedic implants: A review, *Biomaterials* 83 (2016) 127-141.
- [34] A.G. Demir, L. Monguzzi, B. Previtali, Selective laser melting of pure Zn with high density for biodegradable implant manufacturing, *Additive Manufacturing* 15 (2017) 20-28.
- [35] P. Wen, L. Jauer, M. Voshage, Y. Chen, R. Poprawe, J.H. Schleifenbaum, Densification behavior of pure Zn metal parts produced by selective laser melting for manufacturing biodegradable implants, *Journal of Materials Processing Technology* 258 (2018) 128-137.
- [36] M. Montani, A.G. Demir, E. Mostaed, M. Vedani, B. Previtali, Processability of pure Zn and pure Fe by SLM for biodegradable metallic implant manufacturing, *Rapid Prototyping Journal* 23(3) (2017) 514-523.
- [37] B. Song, S. Dong, S. Deng, H. Liao, C. Coddet, Microstructure and tensile properties of iron parts fabricated by selective laser melting, *Optics & Laser Technology* 56 (2014) 451-460.

- [38] H. Fayazfar, M. Salarian, A. Rogalsky, D. Sarker, P. Russo, V. Paserin, E. Toyserkani, A critical review of powder-based additive manufacturing of ferrous alloys: Process parameters, microstructure and mechanical properties, *Materials & Design* 144 (2018) 98-128.
- [39] Y. Li, H. Jahr, K. Lietaert, P. Pavanram, A. Yilmaz, L.I. Fockaert, M.A. Leeflang, B. Pouran, Y. Gonzalez-Garcia, H. Weinans, J.M.C. Mol, J. Zhou, A.A. Zadpoor, Additively manufactured biodegradable porous iron, *Acta Biomaterialia* 77 (2018) 380-393.
- [40] D. Carluccio, A.G. Demir, L. Caprio, B. Previtali, M.J. Bermingham, M.S. Dargusch, The influence of laser processing parameters on the densification and surface morphology of pure Fe and Fe-35Mn scaffolds produced by selective laser melting, *Journal of Manufacturing Processes* 40 (2019) 113-121.
- [41] J. Shin, S. Kim, D. Jeong, H.G. Lee, D. Lee, J.Y. Lim, J. Kim, Finite Element Analysis of Schwarz P Surface Pore Geometries for Tissue-Engineered Scaffolds, *Mathematical Problems in Engineering* 2012 (2012) 13.
- [42] M. Doube, M.M. Kłosowski, I. Arganda-Carreras, F.P. Cordelières, R.P. Dougherty, J.S. Jackson, B. Schmid, J.R. Hutchinson, S.J. Shefelbine, BoneJ: Free and extensible bone image analysis in ImageJ, *Bone* 47(6) (2010) 1076-1079.
- [43] BS International Standard, ISO 13314 Mechanical testing of metals, ductility testing, compression test for porous and cellular metals, BSI, 2011, pp. 1-7.
- [44] A.S.f.T.a. Materials, ASTM G59 - 97: Standard Test Method for Conducting Potentiodynamic Polarization Resistance Measurements, 2014.
- [45] S. Johnston, Z. Shi, A. Atrens, The influence of pH on the corrosion rate of high-purity Mg, AZ91 and ZE41 in bicarbonate buffered Hanks' solution, *Corrosion Science* 101 (2015) 182-192.
- [46] American Society for Testing and Materials, ASTM G1-03: Standard Practice for Preparing, Cleaning, and Evaluating Corrosion Test Specimens, 2017.
- [47] American Society for Testing and Materials, NACE TM0169/G31-12a: Standard Guide for Laboratory Immersion Corrosion Testing of Metals, 2012.
- [48] International Standards Organization, ISO 10993 - 5: 2009. Biological evaluation of medical devices - Part 5: Tests for in vitro cytotoxicity, (2009).
- [49] L.-E. Loh, C.-K. Chua, W.-Y. Yeong, J. Song, M. Mapar, S.-L. Sing, Z.-H. Liu, D.-Q. Zhang, Numerical investigation and an effective modelling on the Selective Laser Melting (SLM) process with aluminium alloy 6061, *International Journal of Heat and Mass Transfer* 80 (2015) 288-300.
- [50] S. Cotes, M. Sade, A.F. Guillermet, Fcc/Hcp martensitic transformation in the Fe-Mn system: Experimental study and thermodynamic analysis of phase stability, *Metallurgical and Materials Transactions A* 26(8) (1995) 1957-1969.
- [51] J. Martínez, S.M. Cotes, A.F. Cabrera, J. Desimoni, A. Fernández Guillermet, On the relative fraction of ϵ martensite in γ -Fe-Mn alloys, *Materials Science and Engineering: A* 408(1) (2005) 26-32.
- [52] Y. Ishikawa, Y. Endoh, Antiferromagnetism of γ - FeMn Alloys, *Journal of Applied Physics* 39(2) (1968) 1318-1319.
- [53] C. Zhao, K. Fezzaa, R.W. Cunningham, H. Wen, F. De Carlo, L. Chen, A.D. Rollett, T. Sun, Real-time monitoring of laser powder bed fusion process using high-speed X-ray imaging and diffraction, *Scientific Reports* 7(1) (2017) 3602.
- [54] M.J. Bermingham, D.H. StJohn, J. Krynen, S. Tedman-Jones, M.S. Dargusch, Promoting the columnar to equiaxed transition and grain refinement of titanium alloys during additive manufacturing, *Acta Materialia* 168 (2019) 261-274.
- [55] T. Schubert, W. Löser, S. Schinnerling, I. Bächer, Alternative phase formation in thin strip casting of stainless steels, *Materials Science and Technology* 11(2) (1995) 181-185.
- [56] D. Buchbinder, H. Schleifenbaum, S. Heidrich, W. Meiners, J. Bültmann, High Power Selective Laser Melting (HP SLM) of Aluminum Parts, *Physics Procedia* 12 (2011) 271-278.
- [57] C.E. Misch, Z. Qu, M.W. Bidez, Mechanical properties of trabecular bone in the human mandible: Implications for dental implant treatment planning and surgical placement, *Journal of Oral and Maxillofacial Surgery* 57(6) (1999) 700-706.

- [58] I. Bogachev, V. Egoiaev, T. Frolova, Features of the Strengthening of Austenitic Fe-Mn Alloys, *Phys. Met. Metallogr.* 33(4) (1972) 127-132.
- [59] D. Carluccio, M. Bermingham, D. Kent, A.G. Demir, B. Previtali, M.S. Dargusch, Comparative Study of Pure Iron Manufactured by Selective Laser Melting, Laser Metal Deposition, and Casting Processes, *Advanced Engineering Materials* 0(0) (2019).
- [60] H.E. Friedrich, B.L. Mordike, *Magnesium technology*, Springer 2006.
- [61] H.F. Li, X.H. Xie, Y.F. Zheng, Y. Cong, F.Y. Zhou, K.J. Qiu, X. Wang, S.H. Chen, L. Huang, L. Tian, L. Qin, Development of biodegradable Zn-1X binary alloys with nutrient alloying elements Mg, Ca and Sr, *Scientific Reports* 5 (2015) 10719.
- [62] Y. Deng, Y. Yang, C. Gao, P. Feng, W. Guo, C. He, J. Chen, C. Shuai, Mechanism for corrosion protection of β -TCP reinforced ZK60 via laser rapid solidification, *International Journal of Bioprinting*; Vol 4, No 1 (2018) (2018).
- [63] K.A. Athanasiou, C. Zhu, D.R. Lanctot, C.M. Agrawal, X. Wang, Fundamentals of biomechanics in tissue engineering of bone, *Tissue engineering* 6(4) (2000) 361-81.
- [64] J.-Y. Rho, L. Kuhn-Spearing, P. Zioupos, Mechanical properties and the hierarchical structure of bone, *Medical Engineering & Physics* 20(2) (1998) 92-102.
- [65] E.F. Morgan, T.M. Keaveny, Dependence of yield strain of human trabecular bone on anatomic site, *Journal of Biomechanics* 34(5) (2001) 569-577.
- [66] S. Pal, *Mechanical Properties of Biological Materials*, in: S. Pal (Ed.), *Design of Artificial Human Joints & Organs*, Springer US, Boston, MA, 2014, pp. 23-40.
- [67] R. Tolouei, J. Harrison, C. Paternoster, S. Turgeon, P. Chevallier, D. Mantovani, The use of multiple pseudo-physiological solutions to simulate the degradation behavior of pure iron as a metallic resorbable implant: a surface-characterization study, *Physical Chemistry Chemical Physics* 18(29) (2016) 19637-19646.
- [68] D. Carluccio, M. Bermingham, D. Kent, A.G. Demir, B. Previtali, M.S. Dargusch, Comparative Study of Pure Iron Manufactured by Selective Laser Melting, Laser Metal Deposition, and Casting Processes, *Advanced Engineering Materials* 21(7) (2019) 1900049.
- [69] E.M.A. Martini, I.L. Muller, Characterization of the film formed on iron in borate solution by electrochemical impedance spectroscopy, *Corrosion Science* 42(3) (2000) 443-454.
- [70] L.P. Lefebvre, J. Banhart, D.C. Dunand, Porous Metals and Metallic Foams: Current Status and Recent Developments, *Advanced Engineering Materials* 10(9) (2008) 775-787.
- [71] T. Yamamoto, K. Fushimi, S. Miura, H. Konno, Influence of substrate dislocation on passivation of pure iron in pH 8.4 borate buffer solution, *Journal of The Electrochemical Society* 157(7) (2010) C231-C237.
- [72] M. Peuster, C. Hesse, T. Schloo, C. Fink, P. Beerbaum, C. von Schnakenburg, Long-term biocompatibility of a corrodible peripheral iron stent in the porcine descending aorta, *Biomaterials* 27(28) (2006) 4955-4962.
- [73] H. Hermawan, A. Purnama, D. Dube, J. Couet, D. Mantovani, Fe-Mn alloys for metallic biodegradable stents: Degradation and cell viability studies, *Acta Biomaterialia* 6(5) (2010) 1852-1860.
- [74] P.K. Mattila, P. Lappalainen, Filopodia: molecular architecture and cellular functions, *Nature Reviews Molecular Cell Biology* 9 (2008) 446.
- [75] K. Anselme, Osteoblast adhesion on biomaterials, *Biomaterials* 21(7) (2000) 667-681.